

## Supporting information:

# All-scale hierarchical thermoelectrics: MgTe in PbTe facilitates valence band convergence and suppresses bipolar thermal transport for high performance

Li-Dong Zhao,<sup>1</sup> Haijun Wu,<sup>2</sup> Shiqiang Hao,<sup>3</sup> Chun-I Wu,<sup>4</sup> Xiaoyuan Zhou,<sup>5</sup> Kanishka Biswas,<sup>1</sup> Jiaqing He,<sup>2,\*</sup> Timothy P. Hogan,<sup>4</sup> Ctirad Uher,<sup>5</sup> C. Wolverton,<sup>3</sup> Vinayak P. Dravid,<sup>3</sup> and Mercouri G. Kanatzidis<sup>1,\*</sup>

<sup>1</sup>Department of Chemistry, Northwestern University, Evanston, Illinois 60208, United States

<sup>2</sup>Department of Physics, South University of Science and Technology of China, Shenzhen 518055, China

<sup>3</sup>Department of Materials Science and Engineering, Northwestern University, Evanston, Illinois 60208, United States

<sup>4</sup>Department of Electrical and Computer Engineering, Michigan State University, East Lansing, Michigan 48824, United States

<sup>5</sup>Department of Physics, University of Michigan, Ann Arbor, Michigan, 48109, United States

\*Corresponding authors: he.jq@sustc.edu.cn; m-kanatzidis@northwestern.edu

## Experimental details:

**Sample preparations:** To prepare for SPS processing, the melt grown ingots were ground to powder using a mortar and pestle to reduce the grain size to smaller than  $5\text{ mm}^3$  and then further ground by a mechanical mortar and pestle to reduce the grains to less than  $53\text{ }\mu\text{m}^3$ . These powders were then densified at 823 K for 10 min in a 20 mm diameter graphite die under an axial compressive stress of 60 MPa in an argon atmosphere. Highly dense disk-shaped pellets with dimensions of 20 mm (diameter)  $\times$  9 mm (thickness) were obtained. The manipulations and preparative steps for the grinding powders were carried out in a purified Ar-atmosphere glove box. The obtained samples were sealed inside an evacuated silica tube with a pressure of  $\sim 10^{-4}$  torr and annealed at 823 K for 15 d to evaluate their thermal stability.

**Band gap measurements:** Room temperature optical diffuse reflectance measurements were performed on finely ground powders to probe optical energy gap of the series. The spectra were collected in the mid-IR range ( $6000\text{--}400\text{ cm}^{-1}$ ) using a Nicolet 6700 FT-IR spectrometer. The reflectance versus wavelength data generated, were used to estimate the band gap by converting reflectance to absorption data according to Kubelka-Munk equations:  $a/S = (1-R)^2/(2R)$ , where  $R$  is the reflectance,  $a$  and  $S$  are the absorption and scattering coefficients, respectively.

**Electrical properties:** The obtained SPS processed pellets were cut into bars with dimensions 18 mm  $\times$  3 mm  $\times$  3 mm that were used for simultaneous measurement of the Seebeck coefficient and the electrical conductivity using an Ulvac Riko ZEM-3 instrument under a helium atmosphere from room temperature to 923 K. The samples were coated with a thin layer (0.1-0.2 mm) of boron nitride (BN) to protect instruments. Heating and cooling cycles gave repeatable electrical properties to verify the thermal stability. The uncertainty of the Seebeck coefficient and electrical conductivity measurements is 5%.

**Hall measurements:** Room Hall coefficients were measured on a home-built system in magnetic fields ranging from 0 to 1.25 T, utilizing simple four-contact Hall-bar geometry, in both negative and positive polarity to eliminate Joule resistive errors. High temperature Hall coefficients were measured with a homemade high temperature apparatus, which provides a working range from 300 to 723 K. The sample was press mounted and protected with argon gas to avoid possible oxidation at high temperature. The Hall resistance was monitored with a Linear Research AC

Resistance Bridge (LR-700), with constant magnetic fields of  $\pm 1$  T applied by using an Oxford Superconducting Magnet.

**Thermal conductivity:** High density SPS processed pellets were cut and polished into coins of  $\varnothing \sim 8$  mm and 1-2 mm thickness for thermal diffusivity measurements. The samples were coated with a thin layer of graphite to minimize errors from the emissivity of the material. The thermal conductivity was calculated from  $\kappa = D \cdot C_p \cdot \rho$ , where the thermal diffusivity coefficient ( $D$ ) was measured using the laser flash diffusivity method in a Netzsch LFA457, the specific heat capacity ( $C_p$ ) was indirectly derived using a representative sample (Pyroceram 9606) in the range 300-923K, the  $C_p$  results show good agreement with the reported values. The density ( $\rho$ ) was determined using the dimensions and mass of the sample, which was then reconfirmed using a gas pycnometer (Micromeritics AccuPyc1340) measurements. The thermal diffusivity data were analyzed using a Cowan model with pulse correction and heating and cooling cycles give reproducible values for each sample. The uncertainty of the thermal conductivity is estimated to be within 5%, considering the uncertainties for  $D$ ,  $C_p$  and  $\rho$ . The combined uncertainty for all measurements involved in the calculation of  $ZT$  is about 15%. No directional anisotropy effects were observed in the thermoelectric transport properties through measurements in transverse and longitudinal directions. The density, heat capacity and thermal diffusivity for all samples can be found in the Table S1 and Figure S1.

**Electron microscopy and X-ray diffraction:** Transmission electron microscopy (TEM) investigations were carried out in a JEOL 2100F microscope operated at 200 kV. The thin TEM specimens were prepared by conventional methods, the procedures were performed including the cutting, grinding, dimpling, polishing and Ar-ion milling in a liquid nitrogen environment. High-resolution images were simulated with the MacTempas program code with the following parameters as input: Spherical aberration of 1 mm, defocus spread of 8 nm, semiconvergence angle of illumination of 0.55 mrad, and a  $7 \text{ nm}^{-1}$  diameter of the objective lens' aperture. Samples pulverized with an agate mortar were used for powder X-ray diffraction (XRD). The powder diffraction patterns were obtained with Cu K $\alpha$  ( $\lambda=1.5418\text{\AA}$ ) radiation in a reflection geometry on an Inel diffractometer operating at 40 kV and 20 mA and equipped with a position-sensitive detector.

**Band structure calculations:** To investigate band energies for the conduction band and valence bands ( $L$  and  $\Sigma$  bands), we consider rocksalt primitive cell of PbTe and different concentration of Mg

addition at ~ 1.0 % ( $\text{Pb}_{124}\text{Mg}_1\text{Te}_{125}$ ) and ~ 4.0 % ( $\text{Pb}_{26}\text{Mg}_1\text{Te}_{27}$ ) to investigate band change upon ternary solution. The calculations were performed using the local gradient approximation with ultrasoft pseudopotentials as implemented in VASP (Vienna Ab-initio Simulation Package).<sup>1-3</sup> All structures are fully relaxed with respect to cell vectors and cell-internal positions. Beside a primitive rocksalt band structure as a control sample, we are using  $5 \times 5 \times 5$  and  $3 \times 3 \times 3$  supercells of the rocksalt primitive cell with one Mg atom substitution for Pb atom to represent above two different concentrations respectively. The zone samplings are adopted using a  $16 \times 16 \times 16$ ,  $1 \times 1 \times 1$  and  $2 \times 2 \times 2$   $k$ -point mesh for each of above concentrations. A uniform 458 eV cutoff energy is applied for all cases. After relaxation, the energy level of  $L$ -point and  $\Sigma$ -line and corresponding energy differences can be calculated. It is worth noting that the test calculations on PbTe,  $\text{Pb}_{124}\text{Mg}_1\text{Te}_{125}$  and  $\text{Pb}_{26}\text{Mg}_1\text{Te}_{27}$  with spin-polarization for  $L$  and  $\Sigma$  bands energies indicated that band structures are the same as non-spin polarization results. The band structures for PbTe,  $\text{Pb}_{0.99}\text{Mg}_{0.01}\text{Te}$  and  $\text{Pb}_{0.96}\text{Mg}_{0.04}\text{Te}$  can be found in the Figure S2.

**Sample density measurements:** For coin-shaped samples analyzed for thermal diffusivity, sample densities were calculated using sample volume as measured using a digital caliper and mass measured on a 4 digit balance, the measured density was then reconfirmed using a gas pycnometer (Micromeritics AccuPyc1340) measurements. Using established densities of PbTe of 8.24 g/cc [4] and MgTe of 3.65 g/cc. [5] The theoretical density  $\rho(x)$  of the  $\text{PbTe} + y$  at.%  $\text{MgTe}$  ( $y = 0, 1, 2, 4, 5, 6$ , and 8) samples were calculated using the law of mixtures:

$$\rho(x) = (1 - x)\rho_{\text{PbTe}} + x\rho_{\text{MgTe}} \quad (1)$$

where  $x$  is volume fraction. [6]

Because the Na alloys completely within the PbTe phases, we do not include Na doping in the final calculations of density. Table S1 shows sample densities for the samples in this report.

**Table S1.** Density of samples included in the study.

Composition	Theoretical Density, g/cc	Measured Density, g/cc	% Theoretical Density
Pb <sub>0.98</sub> Na <sub>0.02</sub> Te	8.2400	7.9833	96.88
Pb <sub>0.98</sub> Na <sub>0.02</sub> Te + 1% MgTe	8.1932	7.9947	97.57
Pb <sub>0.98</sub> Na <sub>0.02</sub> Te + 2% MgTe	8.1464	7.8551	96.42
Pb <sub>0.98</sub> Na <sub>0.02</sub> Te + 4% MgTe	8.0528	7.8876	97.94
Pb <sub>0.98</sub> Na <sub>0.02</sub> Te + 5% MgTe	8.0060	7.9800	99.67
Pb <sub>0.98</sub> Na <sub>0.02</sub> Te + 6% MgTe	7.9592	7.7827	97.78
Pb <sub>0.98</sub> Na <sub>0.02</sub> Te + 8% MgTe	7.8656	7.6753	97.58

**Calculation of lattice thermal conductivity:** In order to understand the intrinsic relationship between the low lattice thermal conductivity and high thermoelectric performance of Pb<sub>0.98</sub>Na<sub>0.02</sub>Te + 6% MgTe with its special hierarchical structure from atomic-scale point defect, nanoscale MgTe precipitates and meso-scale grains, we performed a modified theoretical calculation based on Callaway's model.[7] The lattice thermal conductivity can be expressed as:

$$\kappa_{lat} = \frac{k_B}{2\pi^2 v} \left( \frac{k_B T}{\hbar} \right)^3 \int_0^{\theta_D/T} \tau_c \frac{x^4 e^x}{(e^x - 1)^2} dx \quad (2)$$

where the  $\kappa_B$  is the Boltzmann constant,  $\hbar$  is Plank's reduced constant,  $v$  is an average sound (phonon-group) velocity,  $\theta_D$  the Debye temperature, and  $x$  is defined as  $\hbar\omega/\kappa_B T$ .  $\tau_c$  is the combined relaxation time, based on TEM studies, which relates the phonon scattering from Umklapp process ( $\tau_U$ ), normal processes ( $\tau_N$ ), dislocations ( $\tau_D$ ), strain ( $\tau_S$ ), point defect due to solid solution ( $\tau_{PD}$ ), nanoscle precipitates ( $\tau_P$ ), and grain boundaries ( $\tau_B$ ), respectively. Thus the overall relaxation time can be given as:[8]

$$\tau_c^{-1} = \tau_U^{-1} + \tau_N^{-1} + \tau_D^{-1} + \tau_S^{-1} + \tau_{PD}^{-1} + \tau_P^{-1} + \tau_B^{-1} \quad (3)$$

**Table S2.** Input parameters for calculation of relaxation time of phonon scattering for  $\text{Pb}_{0.98}\text{Na}_{0.02}\text{Te}+6\% \text{MgTe}$ .

Relaxation time	Parameter	Symbol [unit]	Value
$\tau_U^{-1} \approx \frac{\hbar\gamma^2}{Mv^2\theta_D} \omega^2 T \exp(-\theta_D/3T)$	Grüneisen parameter of PbTe	$\gamma$	1.96
	Average sound velocity of PbTe	$v$ [m/s]	1770
	Debye temperature of PbTe	$\theta_D$ [K]	136
	Average mass of an atom of PbTe	$M$ [kg]	$2.7767 \times 10^{-25}$
$\tau_N^{-1} \approx \beta\tau_U^{-1}$	Ratio of normal phonon scattering to Umklapp scattering	$B$	2.5
$\begin{aligned} \tau_D^{-1} \approx \eta_D N_d \frac{V_0^{4/3}}{v^2} \omega^3 \\ + \frac{2^{3/2}}{3^{7/2}} \eta_D N_d B_d^2 \gamma^2 \omega \left\{ \frac{1}{2} + \frac{1}{24} \left( \frac{1-2\nu}{1-\nu} \right)^2 \left[ 1 + \sqrt{2} \left( \frac{v_L}{v_T} \right)^2 \right]^2 \right\} \end{aligned}$	Dislocation density	$N_d$ [ $\text{m}^{-2}$ ]	$\sim 1 \times 10^{14}$
	Volume per atom for PbTe	$V_0$ [ $\text{\AA}^3$ ]	33.69
	Magnitude of Burgers vector	$B_d$ [ $\text{\AA}$ ]	2
	Longitudinal phonon velocity of PbTe	$v_L$ [m/s]	3590
	Transverse phonon velocity of PbTe	$v_T$ [m/s]	1260
$\begin{aligned} \tau_P^{-1} = v(\sigma_s^{-1} + \sigma_l^{-1})^{-1} V_p \\ \sigma_s = 2\pi R^2 \\ \sigma_l = \pi R^2 \frac{4}{9} (\Delta D/D)^2 (\omega R/v)^4 \end{aligned}$	Average radius of nanoscale precipitates	$R$ [nm]	2.25
	Mass density of PbTe	$D_{\text{PbTe}}$ [kg/m <sup>3</sup> ]	8164
	Mass density of MgTe	$D_{\text{MgTe}}$ [kg/m <sup>3</sup> ]	4717
	Number density of nanoscale precipitates	$V_p$ [m <sup>-3</sup> ]	$2.12 \times 10^{23}$
$\tau_S^{-1} \approx \frac{144s\gamma^2\varepsilon_m^2r_0^4}{v} \omega^2$ $\tau_{PD}^{-1}$ described in the text	Misfit between the matrix and the precipitate	$\varepsilon_0$	0.07
	Phenomenological parameter of PbTe	$E$	65
	Mass of an atom Pb	$M_{\text{Pb}}$ [amu]	207.2
	Te	$M_{\text{Te}}$	127.6
	Mg	$M_{\text{Mg}}$	24.305
	Radius of an atom Pb	$r_{\text{Pb}}$ [pm]	175
	Te	$r_{\text{Te}}$	140
	Mg	$r_{\text{Mg}}$	150
	Fractional occupant	$f_{\text{Pb}}$ $f_{\text{Te}}$ $f_{\text{Mg}}$	0.96 1 0.04
	Degeneracy	$c_1, c_2$	1

## References:

- [1] Perdew, J. P.; Burke, K. Ernzerhof M. Generalized gradient approximation made simple. *Physical Review Letters* **1996**, *77*, 3865.
- [2] Blochl, P. E. Projector augmented-wave method. *Phys. Rev. B* **1994**, *50*, 17953.
- [3] Kresse, G. & Furthmüller, J. Efficient iterative schemes for ab initio total-energy calculations using a plane-wave basis set. *Phys. Rev. B* **1996**, *54*, 11169.
- [4] Noda, Y.; Ohba, S.; Sato, S.; Saito, Y. *Acta Crystallographica B* **1983**, *39*, 312.
- [5] El haj Hassan, F.; Amrani, B. *Journal of Physics: Condensed Matter* **2007**, *19*, 386234.
- [6] Girard, S. N.; He, J. Q.; Zhou, X. Y.; Shoemaker, D.; Jaworski, C. M.; Uher, C.; Dravid, V. P.; Heremans, J. P.; Kanatzidis, M. G. *J. Am. Chem. Soc.* **2011**, *133*, 16588.
- [7] Callaway, J. *Phys. Rev.* **1959**, *113*, 1046.
- [8] He, J. Q., Girard, S. N., Kanatzidis, M. G. & Dravid, V. P. *Adv. Func. Mater.* **2010**, *20*, 764.

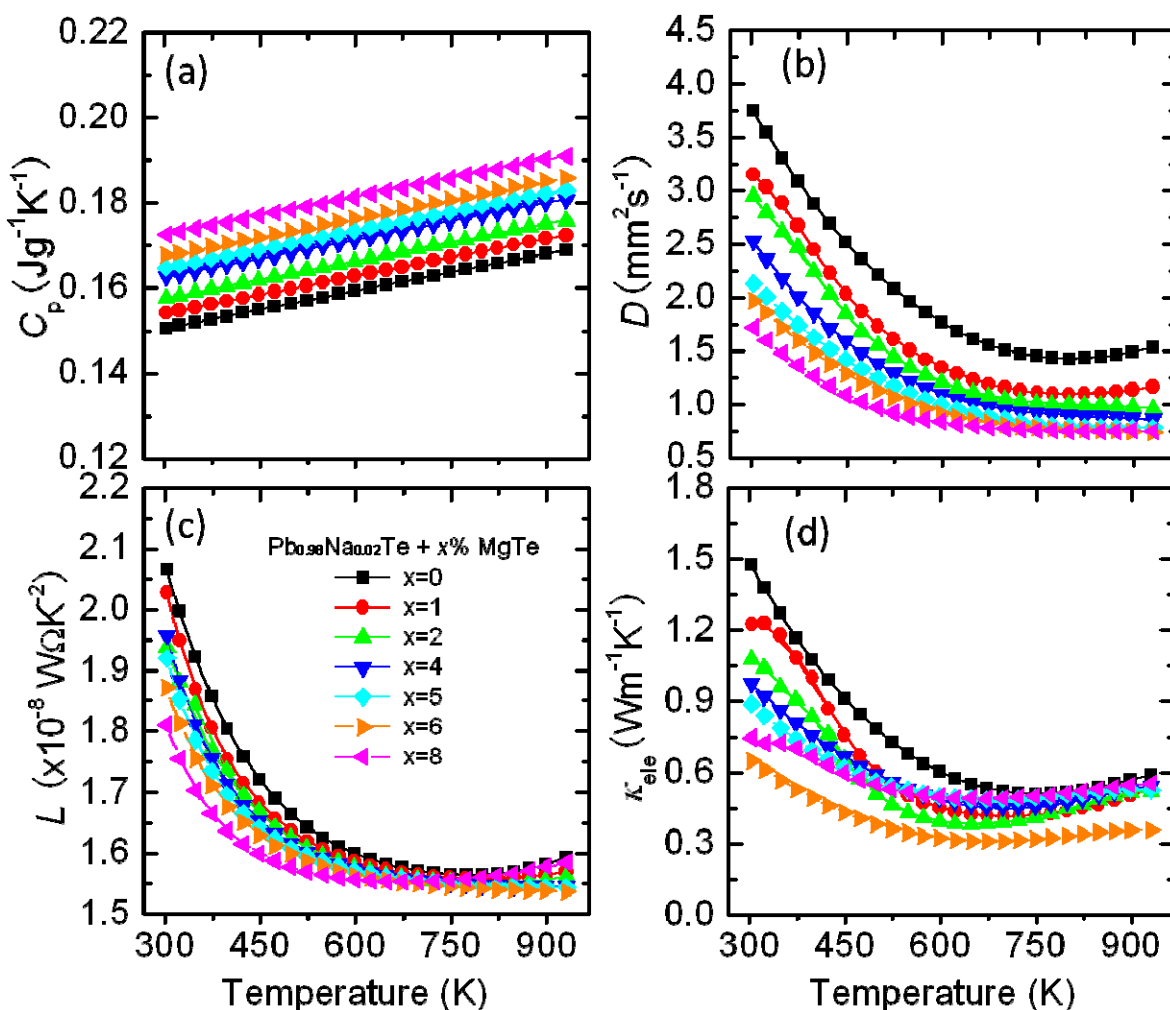


**Figure S1:** Thermoelectric properties as a function of temperature for  $\text{Pb}_{0.98}\text{Na}_{0.02}\text{Te} + x\% \text{ MgTe}$ : (a) Heat capacity; (b) Thermal diffusivity; (c) Lorenz number; (d) Electronic thermal conductivity.

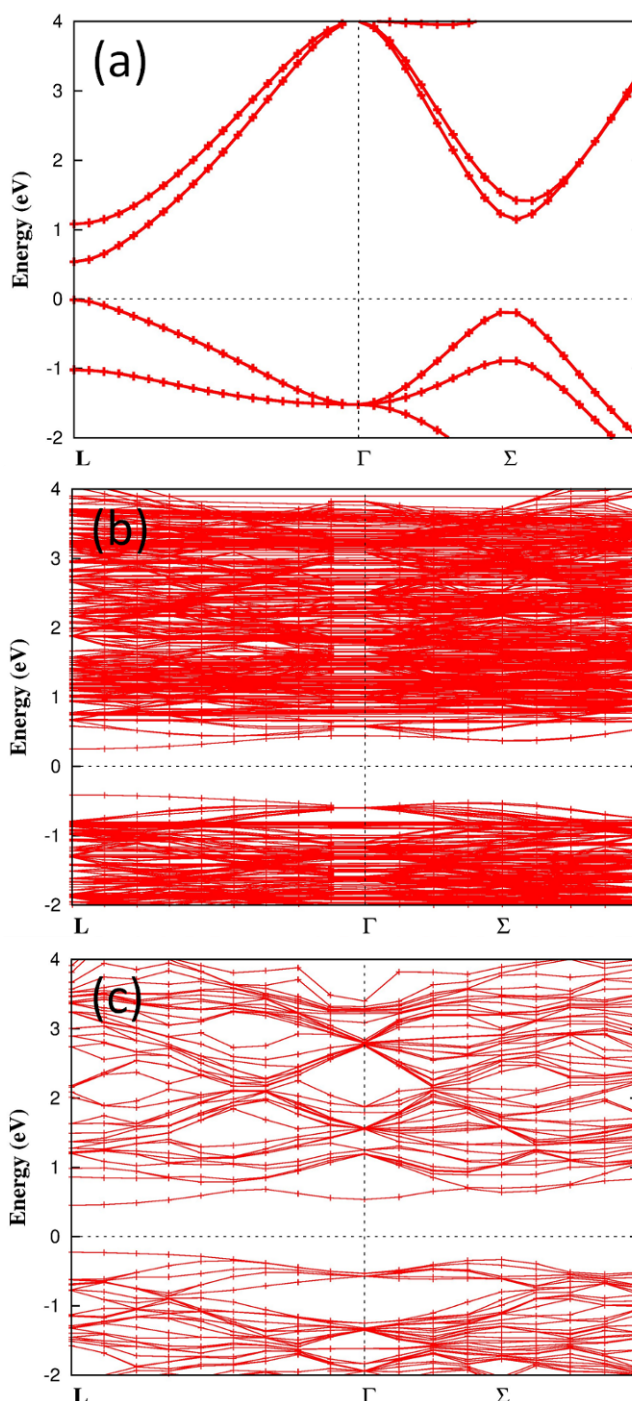


**Figure S2.** The band structure calculations for (a) PbTe, (b)  $\text{Pb}_{0.99}\text{Mg}_{0.01}\text{Te}$  and (c)  $\text{Pb}_{0.96}\text{Mg}_{0.04}\text{Te}$ . All structures are fully relaxed with respect to cell vectors and cell-internal positions. We use  $5 \times 5 \times 5$  and  $3 \times 3 \times 3$  supercells of the rocksalt primitive cell with one Mg atom substitution for a Pb atom to represent above two different concentrations respectively. The  $k$ -point integrations are performed using a  $16 \times 16 \times 16$  mesh for the primitive rocksalt cell, and  $1 \times 1 \times 1$  and  $2 \times 2 \times 2$   $k$ -point meshes for the  $5 \times 5 \times 5$  and  $3 \times 3 \times 3$  supercells, respectively. A uniform 458 eV cutoff energy is applied for all cases.

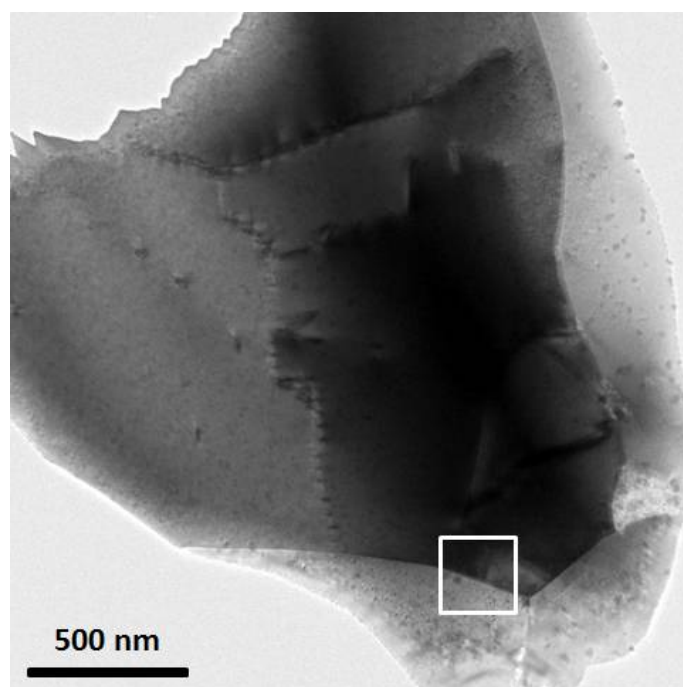


**Figure S3:** Low-magnification TEM image shows grains, the area marked with white line is corresponding to Figure 5 (d).

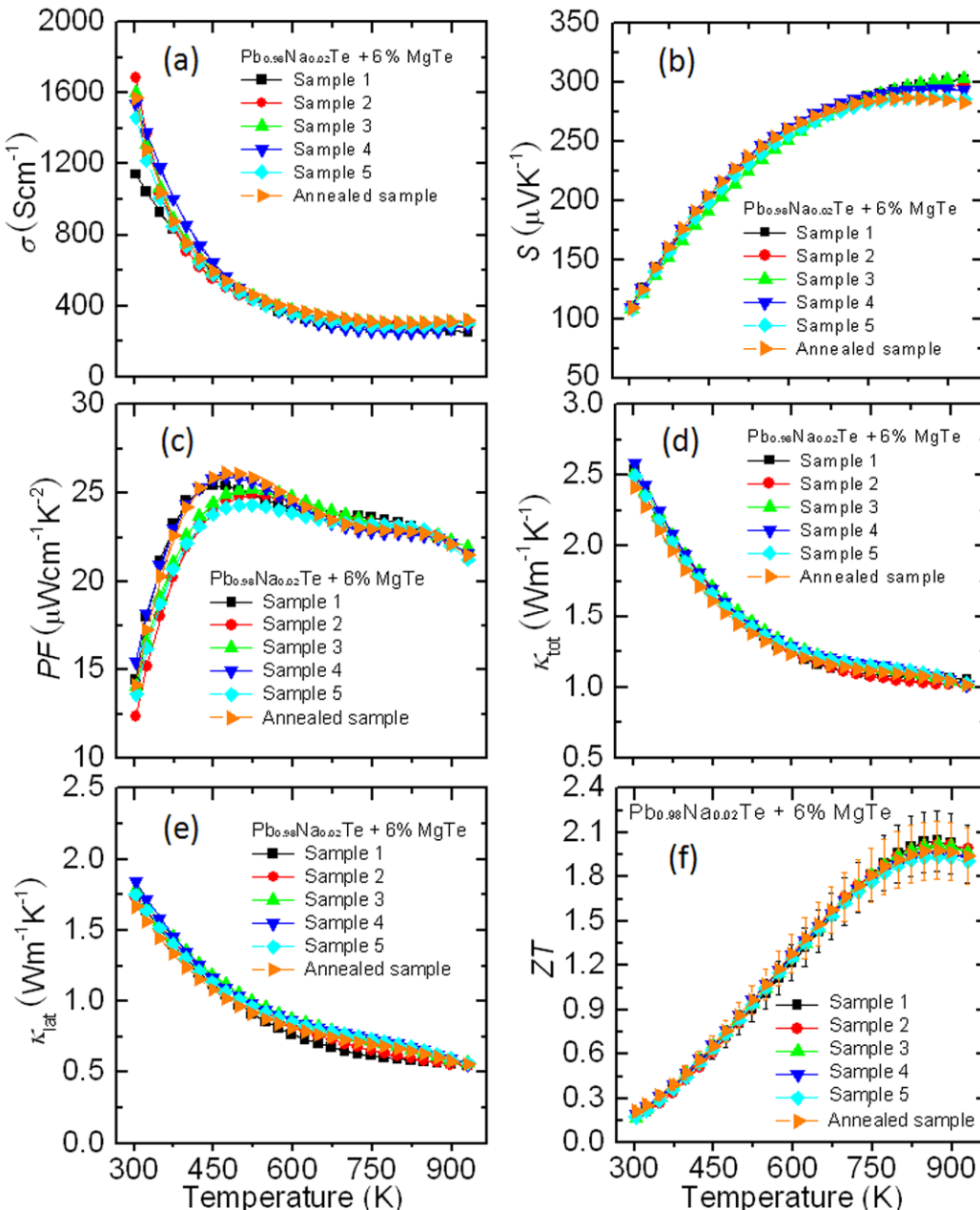


**Figure S4:** Thermoelectric properties as a function of temperature for five samples with same nominal composition of  $\text{Pb}_{0.98}\text{Na}_{0.02}\text{Te} + 6\% \text{MgTe}$  and one sample annealed at 873K for 2 weeks,: (a) Electrical conductivity, (b) Seebeck coefficient, (c) Power factor, (d) Total thermal conductivity, (e) Lattice thermal conductivity and (f) ZT, the combined uncertainty for all measurements involved in the calculation of ZT is less than 15%. Results indicate a good experimental repeatability and thermal stability for the high performance  $\text{Pb}_{0.98}\text{Na}_{0.02}\text{Te} + 6\% \text{MgTe}$ . Actually, besides annealing treatments, the thermal stability was also evidenced from the fact that the heating and cooling cycles on the measurements gave repeatable thermoelectric properties.

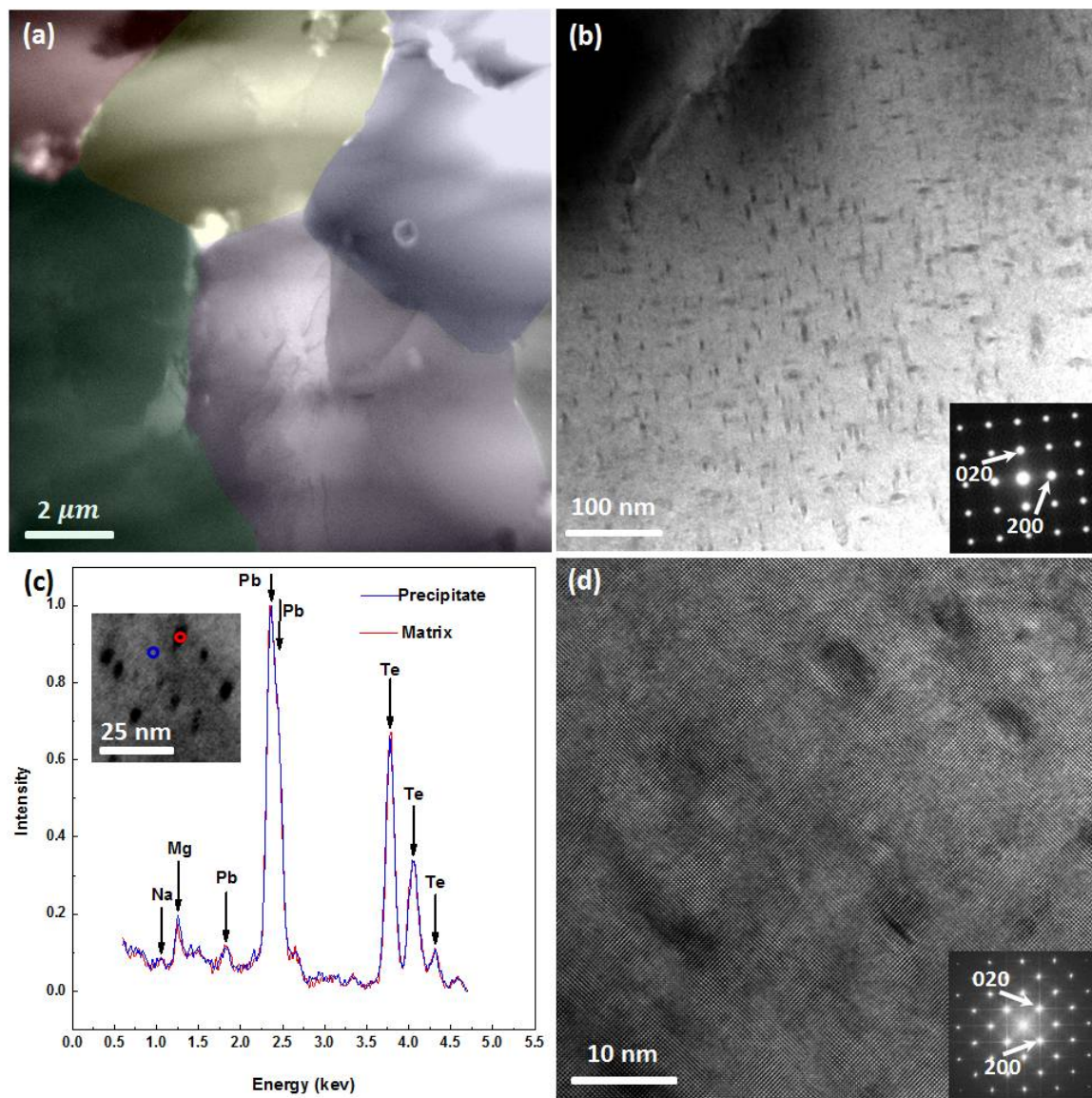


**Figure S5:** (a) Low-magnification TEM image reveals grains in  $\text{Pb}_{0.98}\text{Na}_{0.02}\text{Te} + 6\%$   $\text{MgTe}$  annealed at 873K for 2 weeks. (b) Medium-magnification TEM image depicts presence of spherical/ellipsoidal nanoscale precipitates. The inset electron diffraction pattern in (b) confirms the crystallographic alignment of  $\text{MgTe}$  in the  $\text{PbTe}$  lattices. (c) Comparison of EDS spectrum between precipitate (blue) and matrix (red) comes from inset STEM image. (d) High-magnification lattice image depicting plate-like and spherical/ellipsoidal precipitates, the inset FFT image confirms the endotaxially aligned structure between  $\text{MgTe}$  precipitate and  $\text{PbTe}$  matrix. TEM studies of the annealed sample did not reveal significant changes in microstructure and morphology. A slightly smaller precipitate size and larger grain size in the annealed sample was observed, respectively. This may be due to the Mg dissolving into the matrix and the thermodynamic drive force for grain growth during annealing.